



## Discovery of the deep-sea NEOM Brine Pools in the Gulf of Aqaba, Red Sea

Sam J. Purkis<sup>1</sup>  , Hannah Shernisky<sup>1</sup>, Peter K. Swart<sup>1</sup>, Arash Sharifi<sup>1,2</sup>, Amanda Oehlert<sup>1</sup>, Fabio Marchese<sup>3</sup>, Francesca Benzoni<sup>3</sup>, Giovanni Chimienti<sup>4</sup>, Gaëlle Duchâtellier<sup>1</sup>, James Klaus<sup>1</sup>, Gregor P. Eberli<sup>1</sup>, Larry Peterson<sup>1</sup>, Andrew Craig<sup>5</sup>, Mattie Rodrigue<sup>5</sup>, Jürgen Titschack<sup>6</sup>, Graham Kolodziej<sup>7</sup> & Ameer Abdulla<sup>8</sup>

Deep-sea brine pools represent hypersaline environments famed for their extremophile microbes. With anoxia entirely excluding bioturbating megafauna, brine pools are also conducive to the pristine preservation of sedimentary sequences. Here we use bathymetric and geophysical observations to locate a complex of brine pools in the Gulf of Aqaba consisting of one 10,000 m<sup>2</sup> pool and three minor pools of less than 10 m<sup>2</sup>. We further conduct sediment coring and direct sampling of the brine to confirm the sedimentary and environmental characteristics of these pools. We find that the main pool preserves a stratigraphy which spans at least 1200 years and contains a combination of turbidites, likely resulting from flashfloods and local seismicity, and tsunamigenic terrestrial sediment. The NEOM Brine Pools, as we name them, extend the known geographical range of Red Sea brine pools, and represent a unique preservational environment for the sedimentary signals of regional climatic and tectonic events.

<sup>1</sup>CSL - Center for Carbonate Research, Department of Marine Geosciences, Rosenstiel School of Marine and Atmospheric Science, University of Miami, Miami, FL 33149, USA. <sup>2</sup>Beta Analytic Inc., Isobar Science, Miami, FL, USA. <sup>3</sup>Red Sea Research Center, Division of Biological and Environmental Science and Engineering, King Abdullah University of Science and Technology, Thuwal, Saudi Arabia. <sup>4</sup>Department of Biology and CoNISMA LRU, University of Bari Aldo Moro, Bari, Italy. <sup>5</sup>OceanX, New York, NY, USA. <sup>6</sup>MARUM - Center for Marine Environmental Sciences, Bremen, Germany. <sup>7</sup>CIMAS, Rosenstiel School of Marine and Atmospheric Science, University of Miami, Miami, FL, USA. <sup>8</sup>NEOM, Riyadh, Saudi Arabia. ✉email: [spurkis@rsmas.miami.edu](mailto:spurkis@rsmas.miami.edu)

Deep-sea brine pools are formed by the stable accumulation of hypersaline solutions in seabed depressions. Three water bodies, the Gulf of Mexico, the Mediterranean, and the Red Sea have such conditions and host brine pools<sup>1–7</sup>. Even in these water bodies, brine pools are relatively rare, with only a few tens of discoveries across all three venues. The pools are also tiny compared to their host basins, ranging in size from only hundreds of square meters to a few square kilometers.

Despite their rarity and diminutive size, brine pools present intense oases of macrofaunal and microbial biodiversity in a deep-sea benthic environment that otherwise lacks in number and variety of species<sup>8–18</sup>. Deep-sea brine pools are of intense scientific interest since their pervasive anoxia, low pH, and hypersalinity represent one of the most extreme habitable environments on Earth, perhaps offering clues to first life on our planet, and guiding the search for life beyond it<sup>7,19,20</sup>. The significance of Red Sea brine pools has been further amplified with the discovery that the extremophile microbes that inhabit them can yield bioactive molecules with therapeutic potential, including antibacterial and anticancer properties<sup>21,22</sup>.

Of all the venues of brine pools globally, the Red Sea boasts the highest number and their provenance is traditionally tied to the dissolution of abundant subsurface evaporites which were deposited in structural lows during the Miocene evolution of the rift basin<sup>23–28</sup>. The population of brine pools can be conveniently split into two categories—those situated along the deep (>1000 m) axial trough of the basin and associated with its rift spreading axis, versus those located atop the shallower (<850 m) coastal shelf. In the first category, there are at least 25 complexes of pools developed along the axial trough (Fig. 1). All are anoxic, and all are warmer than the 21.35 °C of ambient Red Sea seawater<sup>4,29,30</sup>. Only two brine pools fall into the second category atop the coastal shelf. Both are located offshore Saudi Arabia—the Thuwal Seeps at 860 m water depth in the central Red Sea and the Afifi Brine Pool at 350 m in the south<sup>12,31,32</sup>. Like the axial pools, this pair is both anoxic, and their hypersaline waters are marginally (<2 °C) warmer than ambient.

During the 2020 research cruise of R/V OceanXplorer, an expedition aimed at exploring and further detailing the deep seabed offshore Saudi Arabia, we discovered a complex of brine pools at 1,770 m depth. Unlike all previous discoveries, these pools situate in the Gulf of Aqaba and are the first discovery outside the Red Sea proper. Here we report on our discovery of the NEOM Brine Pools, named eponymously after this research cruise, which was facilitated by NEOM, a Saudi development

company. Given that these pools were found in a location that had never been reported before, a series of in situ measurements and samples (water, surficial sediment samples, and cores) were collected for the purposes of characterizing the overall physical setting of the pools, their sedimentology, chemistry, and biology. These data were used to determine if the NEOM Brine Pools are representatives of the established categories of Red Sea brine pools, or if they present a new category. A defining feature that separates the NEOM pools from previous Red Sea discoveries is that they are located only 2 km from the coast, significantly closer than the next most shore-proximal Thuwal Seep, situated 25 km offshore<sup>12,31</sup>. Situated as such, the NEOM pools are positioned to receive sediments shed from the coastal zone and therefore have the unique potential to archive historical tsunamis, flashfloods, and seismicity in the Gulf of Aqaba.

## Results

**Physical setting of the NEOM Brine Pools.** The NEOM Brine Pools (Fig. 2) locate in the Gulf of Aqaba at 1770 m depth on the bathyal plain of the Aragonese Deep. This basin is conspicuous in being >800 m deeper than the Gulf's average, and comparable in depth to much of the Red Sea axial trough (Fig. 3). Major strike-slip faults occur along both sides of the Aragonese Deep<sup>33,34</sup>. The east side is confined by the Arona fault and the Aragonese fault bounds to the west. Both faults are strike-slip, though the Aragonese fault also displays a substantial dip-slip component<sup>35</sup>. The bounding fault complex of the deep is completed to the north and south by NNW-trending normal faults (Fig. 3b). This fault geometry has a large extensional component and the Deep is considered a true pull-apart basin<sup>36</sup>, the only such occurrence in the Gulf of Aqaba. Seismicity is common. Earthquakes in the area frequently exceed  $M_w = 5.0$ , including the 1995  $M_w = 7.3$  Nuweiba earthquake which resulted from a partial rupture of the Aragonese fault<sup>37–42</sup>.

Our discovery consists of one large brine pool and three minor pools within 50 m of its borders (Fig. 3c). The main pool elongates parallel to the strike of the coastline, is 260 m long, 70 m wide, and covers an area of 10,000 m<sup>2</sup>. The minor pools are tiny by comparison, all <10 m<sup>2</sup>, and circular in shape, possibly owing to their origin to brine spillover from the main pool, as observed in the Atlantis II Deep axial depression in the Red Sea<sup>43,44</sup>. The NEOM complex lies immediately adjacent to the toe-of-slope of the Saudi Arabian margin. Both the pool and the margin can essentially be considered bound by the Arona fault. So close is the main pool to the margin, that its eastern 'shore' is demarked by

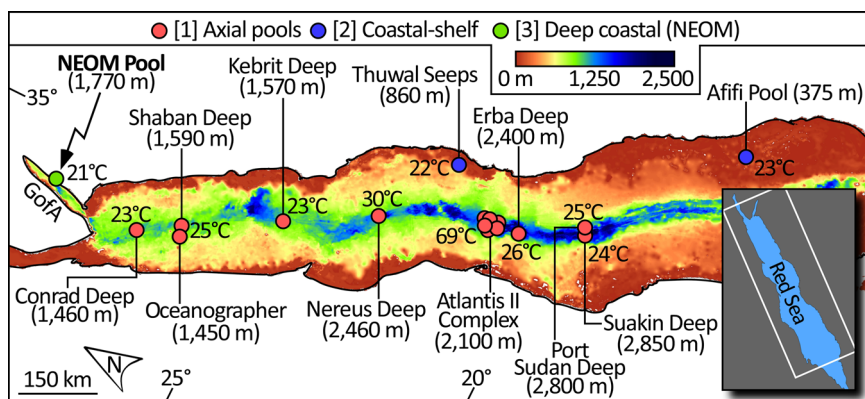


**Fig. 1** Location and temperatures of the Red Sea brine pools. The Red Sea pools split into two convenient categories. [1] Pools in the deep (>1000 m) axial trough associated with the rift spreading axis (red dots). [2] Pools situated on the shallow coastal shelf (0–850 m depth) of the rift (blue dots). The NEOM Brine Pools, the first discovery in the Gulf of Aqaba (GoFA), is neither located on the spreading axis, in the rift basin, nor on the continental shelf (green dot).

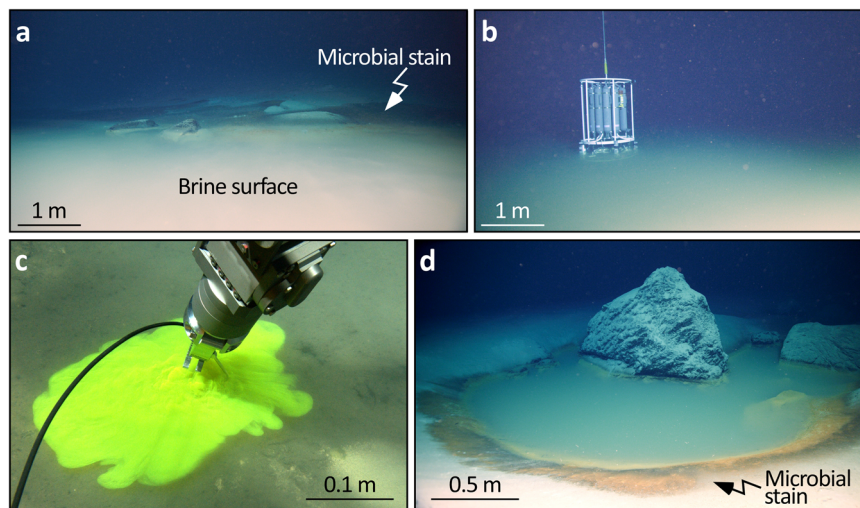


**Fig. 2 Photographs of the NEOM Brine Pools.** **a** Brine surface in the foreground overlaps the “beach” which is characterized by a rich microbial community (orange-to-gray in color). In **b**, at a water depth of 1770 m, a Sea-Bird CTD system is lowered through the brine-seawater interface, a stark transition in density which is especially visible via injection of biodegradable dye (**c**). **d** A small (10 m<sup>2</sup>) brine pool situated 50 m to the west of the main pool and associated with boulders shed from the nearby foreslope. As for the main pool, the microbial community also stains the beach surrounding this small pool.

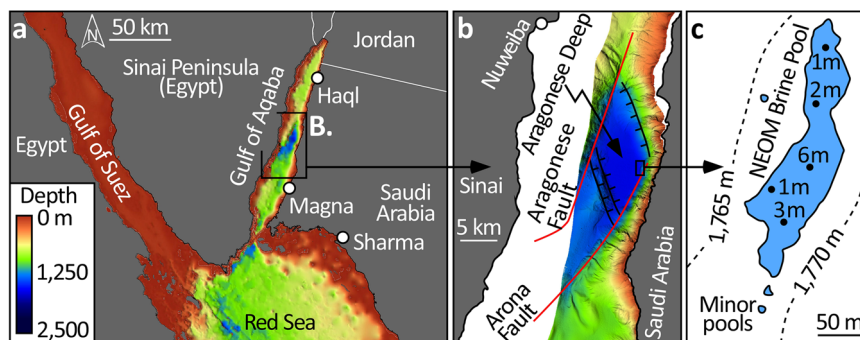


**Fig. 3 Bathymetric and tectonic setting of the NEOM Brine Pools in the Gulf of Aqaba.** **a** The General Bathymetric Chart of the Oceans<sup>90</sup> (GEBCO) provides regional context to the multibeam data acquired during the OceanX-NEOM research cruise (**b**). The brine pool is located at the toe-of-slope of the Saudi coastal margin in the Aragonese Deep, a pull-apart basin and the deepest point in the Gulf. This basin is bounded by the strike-slip Arona and Aragonese faults (red lines) which connect via normal faults (black lines). The NEOM pools situate at the junction between the coast-parallel Arona Fault and the NNW-trending normal fault that extends to demarcate the northern margin of the basin. **c** The brine-seawater interface is at 1770 m depth and the main pool is 260 m long, 70 m wide, and covers an area of 10,000 m<sup>2</sup> (large blue polygon). Echo soundings (black dots) indicate a maximum thickness of the brine to be 6 m in the center of the pool. Three minor pools, each <10 m<sup>2</sup> in area, were discovered within 50 m of the main pool, one westward and two southward (small blue polygons).

the 35° rise of the foreslope. This declivity is maintained up to a water depth of 250 m, shallower than which, the margin steepens to near vertical, prior to terminating at sea level in the form of the crest of the fringing reef that mantles the Saudi coastline of the Gulf of Aqaba.

**Environmental conditions.** The CTD measurements from 1200 m depth, through the brine pool interface (1769.46 m) and 2 m below (1771.50 m) revealed that the bathyal water column above the brine pool has a stable 21.33 °C temperature, the salinity of 40 PSU, and dissolved oxygen of 180 μmol L<sup>-1</sup>. These parameters were constant down to the brine-seawater interface (Fig. 4). Within 15 cm beneath the brine interface, salinity rose from 40 PSU to values higher than the limits of the conductivity probe (120 PSU). Subsequent lab analysis of the brine provided actual salinity values of 160 PSU. Dissolved oxygen values fell more than 75% at the interface, reaching 50 μmol L<sup>-1</sup> by 20 cm submergence into the brine, and further falling to a minimum value of <10 μmol L<sup>-1</sup> by 50 cm below the interface. Given the

limited precision of the probe (±18 μmol L<sup>-1</sup>), such low values can likely be interpreted as fully anoxic, but there remains the possibility that limited mixing of normal Red Sea water into the brine delivers partially anoxic (hypoxic) conditions. Unlike salinity and dissolved oxygen, the temperature did not abruptly change across the brine interface. Instead, the temperature gradually increases below the brine interface at a rate of 0.1 °C per 20 cm depth increase, reaching an increment of 1.0 °C above the temperature of ambient seawater by 2 m depth into the brine (Fig. 4). The temperature differential to ambient did not increase with deeper submergence. Such a modest warming increment suggests the lack of proximal hydrothermal heating of the brine.

**Source of the brine.** The microbes which inhabit the brine-seawater interface provide a convenient proxy to identify point sources for the brine accumulating in the pools. The sediments which host microbes are stained shades of dark gray to orange, thus forming the conspicuous uninterrupted microbial rind around the perimeter of the pools (e.g., Fig. 2a, d). Confirmed by

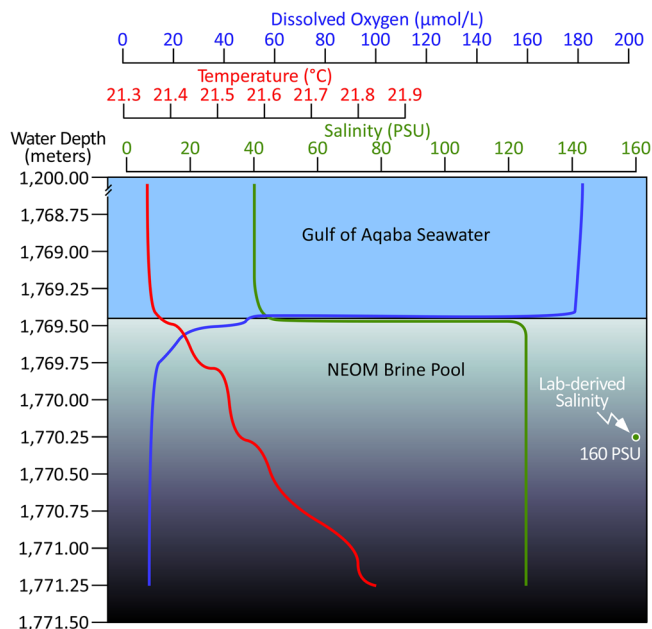


**Fig. 4 Dissolved oxygen, temperature, and salinity profiles into the main NEOM Brine Pool.** The brine-seawater interface is positioned at 1769.46 m water depth (base of blue shading), demarked by the abrupt decrease in dissolved oxygen concentration (blue line) and increase in salinity (green line). Note that the CTD conductivity probe saturated at 120 PSU and the true brine salinity was determined in the lab to be 160 PSU (green dot). The temperature differential between the brine and overlying seawater is  $<1^{\circ}\text{C}$  (red line).

16S rRNA sequencing, the same community was locally observed to extend up-slope above the eastern margin of the pool, suggesting that here too, microbes are colonizing sediments enriched in brine which is welling out of the toe-of-slope (Fig. 5). Such occurrences present as distinct point sources, which broaden downslope as the “curtain” of brine descends into the pool under gravity. The point sources were observed up to 5 m above the surface of the largest NEOM pool with a frequency of one source every two-to-three meters along the entire 260 m stretch of the pool that abuts the slope. The most substantial of these brine seepages were associated with breccia blocks (boulders) which had tumbled to rest on the toe-of-slope (Fig. 5a, c). In some cases, it appeared that these blocks, likely shed from the nearby foreslope, have excavated seabed depressions on the bathyal plain which have subsequently filled with brine (Fig. 2d). The supposition that the microbially-stained curtains are actively nourished by cascading sheets of brine is supported by the abundant colonization of these areas by *Apachecorbula muriatica* Oliver & Vestheim, 2015, a bivalve observed to solely accumulate within the mixing zone between brine and normal seawater around the pools. Further, brine could be visually seen to weep from the toe-of-slope (visible due to shimmering within the water column resultant from the halocline produced by the brine) when the stained sediments were disturbed with the ROV’s manipulator arm. By contrast, brine was not visually evident when non-stained areas in the slope were similarly disturbed.

Given its high density, the possibility of brine being drawn from the pool up the slope via capillary action can be discounted. The only plausible explanation for these observations is that brine seeping from the slope represents one source of brine into the NEOM pool. These seeps must flow continuously, or nearly so, to sustain the halophilic microbial and bivalve communities that inhabit the sediments through which the brine descends into the pool below.

To further examine the provenance of the brine in the NEOM pool, the chemistry of the brine was compared to that of the other Red Sea brines where adequate data exist (Fig. 6a) and to the expected product of evaporating modern Gulf of Aqaba seawater (Fig. 6b). Cross plotting the sulfate/chloride ratio vs. that of sodium/chloride for the largest NEOM pool and its brethren reveals the NEOM pool to separate from the others by virtue of its lower ratios for both sulfate/chloride ( $\text{SO}_4^{2-}/\text{Cl}^-$ ) and sodium/chloride ( $\text{Na}^+/\text{Cl}^-$ ).

This graph assists in the identification of the provenance of the brine, for which there are two plausible mechanisms. The first mechanism is the dissolution of the subsurface evaporitic sequences which are documented to have abundantly accumulated in the Red Sea and its associated gulfs (Aqaba and Suez). These evaporites are generally attributed to the basin’s Late Miocene salinity crisis which occurred early in its rifting phase<sup>23–28</sup>. The second mechanism by which the brine could have conceivably formed is from the subaerial evaporation of modern seawater in coastal sabkhas—e.g., Aref and Mannaa<sup>45</sup>—and the subsequent percolation of the enriched seawater through the coastal shelf prior to accumulation at the bathyal depth of the toe-of-slope.

To the first mechanism, the dissolution of Miocene evaporitic minerals, principally halite, would serve to increase the  $\text{Na}^+/\text{Cl}^-$  ratio from the value of modern Gulf of Aqaba seawater ( $\sim 0.76 \text{ M/M}$ , red dot, top-left, Fig. 6a), to a ratio close to unity (demarcated by a broken vertical line, Fig. 6a). The fact that the population of brine pools, including NEOM, the plot between this pair of endmembers is therefore consistent with their brines being formed by the dissolution of subsurface halite. Like all the other brines discovered in the Red Sea, the NEOM pools show a significant amount of bacterial sulfate reduction. The  $\text{SO}_4^{2-}/\text{Cl}^-$  ratio of the Gulf of Aqaba seawater is  $\sim 50 \text{ mM/M}$  while the NEOM brine has the lowest  $\text{SO}_4^{2-}/\text{Cl}^-$  ratio yet documented in the Red Sea-Gulf of Aqaba system ( $\sim 2 \text{ mM/M}$ ) (Fig. 6a). In this analysis, we assumed that all sulfur measured was present as sulfate, however, given the nearly anoxic conditions of the brine pool, it is likely that some portion was present as  $\text{H}_2\text{S}$ , and thus the  $\text{SO}_4^{2-}/\text{Cl}^-$  ratio would be even lower than shown here.

A subsurface source for the NEOM brine is further upheld by a plot of its stable oxygen isotope measurements versus salinity (Fig. 6b). In this plot, the curved line charts the modeled evaporation of Gulf of Aqaba seawater under a humidity of 50% (annual average for Saudi Arabia). Initializing at 40 PSU and a  $\delta^{18}\text{O}$  value of 2‰, seawater evaporated to the salinity of the NEOM Brine Pool (160 PSU) should have a  $\delta^{18}\text{O}$  value of 16‰. The actual  $\delta^{18}\text{O}$  value of the NEOM brine, meanwhile, is only 1‰, thereby confirming that its brine is not sourced from evaporated modern seawater.

**Lithostratigraphy of the NEOM Brine Pools.** Sampled via a transect of five push cores, a defining characteristic of all the pools in the NEOM complex is the four concentric zones which develop around their rims (Fig. 7). The outermost zone in this series is the hemipelagic mud which constitutes the seabed of the Aragonese Deep. As the brine pool is approached, the second zone encountered is characterized by its rich microbial community which stains the seabed dark gray. This second zone (akin to a beach in a coastal setting) is temporarily inundated by brine when even minor waves were induced into the surface of the pool by the ROV. We, therefore, infer this zone to be episodically inundated with brine under natural conditions too, as the surface is disturbed by the emplacement of brine, megafauna interacting with its surface, or input of slope material into the pool. The gray zone is typically 1–2 m wide, depending on local topography at

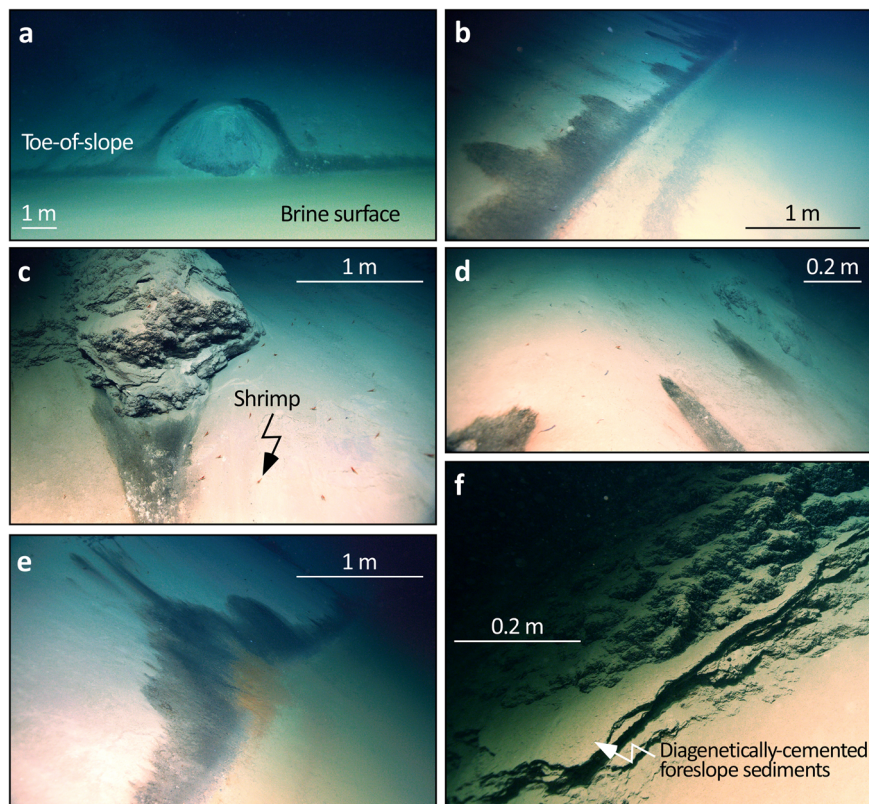


**Fig. 5 Source of the brine.** Microbial staining suggests the main pool is fed by brine released from the toe-of-slope of the eastern margin of the Gulf of Aqaba. This microbial community occupies a niche defined by the presence of hypersaline brine interfacing with oxygenated normal marine waters. Hence, the microbial stain is restricted to the shore of the brine pools and cases where brine emanates from the seabed. **a** Shows a breccia block partially buried in hemipelagic sediment at the toe-of-slope. Microbial stain suggests that this block has mobilized brine from the sediment which flows via gravity into the pool below. **b** Captures brine weeping from the toe-of-slope into the main pool. **c** Shows another breccia block beneath which brine is liberated into the pool. Notice abundant shrimps *Plesionika* sp. (Pandalidae) which were observed scavenging animals stunned or killed by the anoxic brine. In **d, e**, up to 5 m above the pool, brine seeps from the slope. **f** Outcrops from the toe-of-slope 1 m above the pool. The stratigraphy is interleaved with a conspicuous sheeted horizon (arrowed) determined via XRD to be composed of aragonite, high- and low-Mg calcite with a minor contribution of orthoclase feldspar, indicative of enhanced diagenesis of foreslope sediments in the presence of hypersaline waters.

the pool's edge. Third in line, inboard of the gray zone lies the orange “swash” zone which situates immediately at the brine-seawater interface. The orange color is also induced by a dense microbial community. As for the gray zone, we infer this orange zone to be frequently inundated by brine through even the most minor disturbance of the pool's surface. The bivalve *A. muritica* densely inhabits both the gray and orange zones. The fourth zone in the sequence is located within the brine pool proper, which we define as permanently submerged beneath brine.

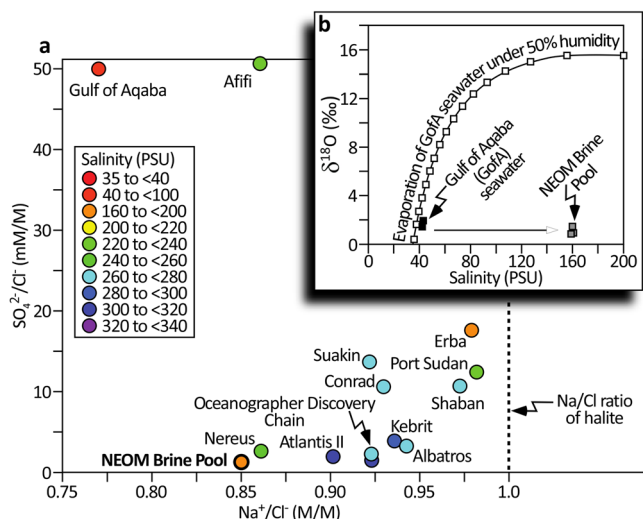
Core #1 penetrates the hemipelagic mud away from the brine and its stratigraphy is disturbed by bioturbation. Cores #2 through 5, by contrast, all acquired beneath the brine-seawater interface, are not bioturbated since the anoxic waters of the brine exclude benthic megafauna. The lack of bioturbation allows for the preservation of mm-scale depositional sequences in the cores acquired beneath the brine (Fig. 7c).

Radiometric dating of bulk sediments sampled from six horizons of the longest core (Core #5) pushed into the bed of the brine pool enabled us to derive an age model spanning 1.2 kyrs of sedimentary deposition (Fig. S2). With the caveat that we cannot unequivocally discount the effect of recycled carbon, no age reversals were observed in the core, suggesting that its record is both undisturbed and continuous. To determine sedimentation rate, we used both Bayesian<sup>46,47</sup> and linear models to generate an age-depth relationship for the core, delivering an average sedimentation rate ranging from 0.5 to

4.5 mm/yr. The core presents three broad motifs of deposition (Fig. 8a–e).

Accounting for 30% of the core, the first depositional motif is a series of rose-colored coarse intervals comprised of angular grains spanning the sand to granule size fraction. As determined via stereomicroscopy, the mineralogy of these intervals is primarily quartz and feldspar, with minor contributions of biotite, chlorite, and muscovite. Maximum carbonate content in these intervals is 10% and can mostly be attributed to occasional pteropods admixed amongst the siliciclastic grains. The most prominent siliciclastic interval is nearly 30 cm thick and, according to the Bayesian age model, was deposited between 525 and 650 yrs. BP. Albeit thinner, seven similarly composed siliciclastic intervals are recorded in the core, of which four date to older than the 30-cm-thick event. From oldest to youngest these are, a 2 cm interval dating to 1050 yrs. BP, and 1 cm intervals at 950, 780, and 700 yrs. BP. Three coarse siliciclastic intervals predate the 30-cm-thick event and situate at 500 yrs (1 cm thick), 390 yrs. BP (2 cm thick), and 50 yrs. BP (4 cm thick).

The second style of deposition and accounting for 55% of the core presents as stacked fining-upward layers which span clay-to-silt textures. These sediments are >30% calcareous, relatively rich in total organic carbon (TOC, 0.4–0.8%), and dark brown to olive in color (Fig. 8f). The layers range in thickness from <0.5 to 4.0 cm. Ubiquitously fining-upward, planar laminations, recognizable sole marks at the coarse base of the intervals, and

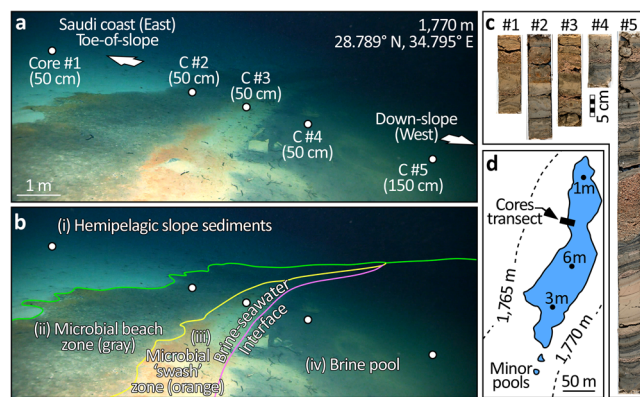


proximity of the pool to the slope distinguish these layers as deposited by turbidity currents.

The final motif of deposition occupies 15% of the core and presents as a single 20-cm-thick interval of tan-colored clay with silt streaks that deposited uninterrupted between 750 and 900 yrs. BP. The carbonate content of this interval of the deposit is the highest recognized in the core at 50–60%.

**Chemostratigraphy of the NEOM Brine Pools.** Downcore variation of elemental intensities measured by XRF-scanning at 2-mm intervals are presented in the form of elemental ratios (Fig. 8j–l) and the combined abundance of quartz and feldspar as determined by XRD presented at 25 mm intervals (Fig. 8m). These data were accompanied by discrete analyses of 27 samples for carbon stable isotope ( $\delta^{13}\text{C}$  values) and TOC (Fig. 8n, o).

Downcore variations of  $\text{Rb}/\text{Zr}$ ,  $(\text{Zr} + \text{Rb})/\text{Sr}$ , and  $\text{K}/\text{Fe}$  indicate at least ten intervals of elevated ratios correlated with coarse-grained siliciclastic turbidite intervals. The  $\text{Rb}/\text{Sr}$  ratios vary from 0.01 to 0.09,  $(\text{Zr} + \text{Rb})/\text{Sr}$  ratios ranged from 0.18 to 1.77, and  $\text{K}/\text{Fe}$  ratios vary from 0.19 to 1.83. Highest  $\text{Rb}/\text{Zr}$ ,  $(\text{Zr} + \text{Rb})/\text{Sr}$ , and  $\text{K}/\text{Fe}$  ratios were observed in the interval from 48 to 77 cm, where the thickest coarse-grained siliciclastic sand layer locates. Based on XRD analysis, downcore abundances of major silicate minerals (quartz + feldspars) varied from 11.4–89.1%, with the highest



values observed in the interval from 48 to 77 cm (Fig. 8m), dating to approximately 600 yrs. BP.

The TOC contents of the thick laminae of dark-colored hemipelagite above and below the 48–77 cm interval range from 0.07 to 0.79% (average = 0.31%,  $n = 27$ ). The minimum TOC values are seen in the 48–77 cm coarse siliciclastic sand interval. Except for this interval, the downcore variation of TOC does not appear to be coherent with the intervals of turbidite layers. The  $\delta^{13}\text{C}$  values (Fig. 8n) vary from  $-21.76\text{‰}$  to  $-19.10\text{‰}$ , with an average of  $-19.71\text{‰}$  ( $n = 27$ ). Although the  $\delta^{13}\text{C}$  values down the core seem to be somewhat correlated with TOC, the overall correlation between these two variables is insignificant ( $r^2 = 0.19$ ). Meanwhile, TOC is strongly correlated with total nitrogen (TN) ( $r^2 = 0.99$ ) (Fig. S3a), indicating that the particulate organic matter in the core is derived from a common source. The TOC/TN ratio ranges from 7.72 to 11.82 with an average of 8.96 ( $n = 27$ ). The organic geochemistry results of 27 samples (from both hemipelagite and turbidite intervals) are grouped based on their  $\delta^{13}\text{C}$  values and TOC/TN ratios (Fig. S3b). Here, most of the samples plot within or close to the marine algae domain<sup>48</sup>, suggesting the organic carbon preserved in the stratigraphy which underlays the brine pool to have solely originated in the marine realm.

**Pool-associated megafauna.** The NEOM Brine Pools host a rich metazoan assemblage. Eels, bigeye houndshark (*Lago omanensis*), and flat fish (likely sharpnose tonguesole cf *Cynoglossus acutirostris*) behaved in a manner consistent with their use of the brine as a feeding strategy (Fig. 9a–c). These predators appeared to deliberately cruise the brine surface and the eel (species as yet unidentified) was observed repeatedly dipping into the brine, presumably to retrieve animals which had been shocked or killed

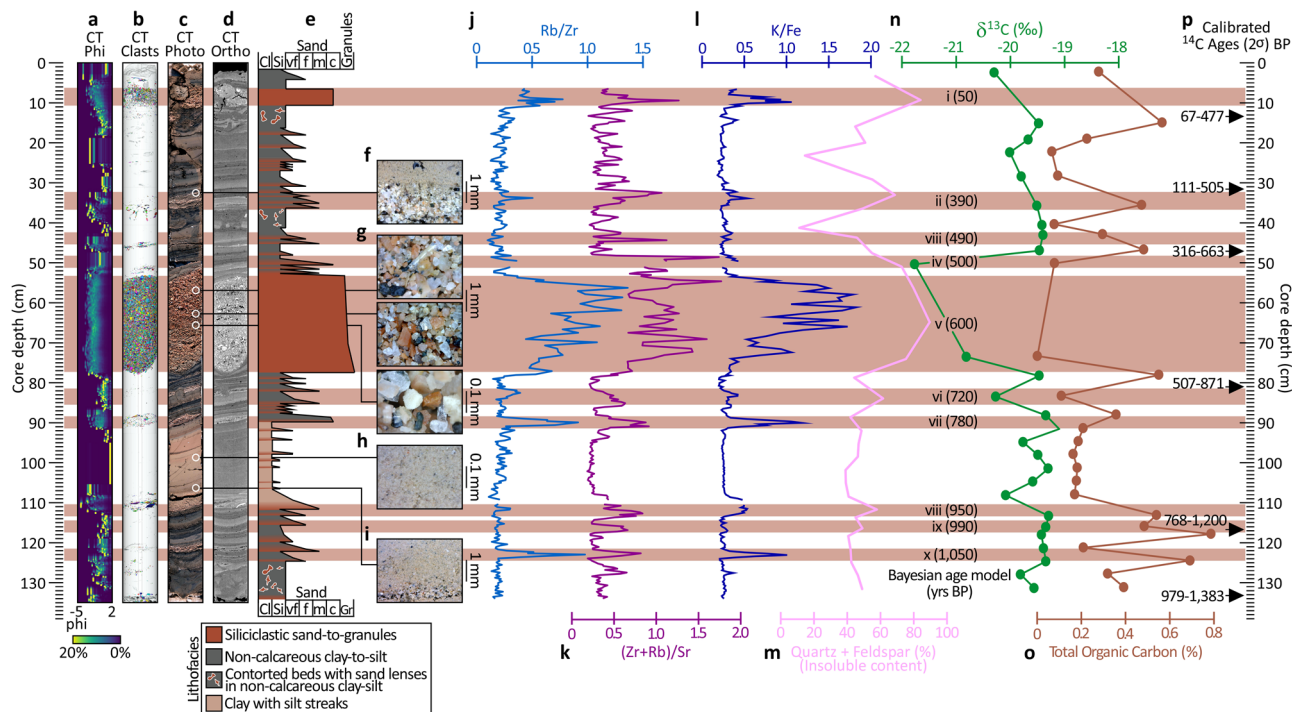


**Fig. 8** Litho- and chemostratigraphy of the 150-cm-long core (Core #5) from the main NEOM Brine Pool. **a** Clast size analysis derived from computed tomography (CT) scanning of the core. In this histogram plot, the left border is  $-5$  phi (i.e., coarse clasts) and the right border is 2 phi (fine clasts). The color scale varies from 0% occurrence of a given phi in 1 cm intervals in blue, up to 20% by volume in yellow. Using random colors, **b** identifies the occurrences of individual clasts. This 3-D visualization excellently emphasizes the ten conspicuous coarse-grained siliciclastic turbidite intervals. Of these, the most prominent is 'v' at 54–77 cm core depth which dates to ~600 yrs. BP. **c** Is a high-resolution digital photo-scan of the split core and **d** is the equivalent grayscale orthoslice reconstructed from CT. **e** Is the core description capturing grain size and lithofacies. **f** through **i** are photomicrographs which detail the fining-upwards arrangement of the turbidite deposits, including coarse siliciclastic intervals (**g**), and the clay deposit with silt streaks during times of uninterrupted deposition (**h**), also interspersed with fining-upwards turbidite deposits (**i**). The chemostratigraphy of the core is captured by variation of elemental intensities measured by XRF-scanning and presented in the form of three ratios: Rb/Zr (**j**), (Zr + Rb)/Sr (**k**), and K/Fe (**l**), and the combined abundance of quartz and feldspar (**m**). These traces are supplemented with discrete analyses of 27 samples for carbon stable isotope ( $\delta^{13}\text{C}$ ) (**n**) and total organic carbon (**o**).  $^{14}\text{C}$  ages calibrated to calendar yrs. BP with  $2\sigma$  error reported (**p**).

by the anoxic waters. Such behavior was unequivocal for the armies of shrimp (*Plesionika* sp.) that amassed on topographic highs around the rim of the pool (Fig. 9d, e). When illuminated by red light, we observed this shrimp species venturing as far as the mid-pool (>30 m from the rim) and plucking out small organisms disabled by the brine (Fig. 9f).

Mirroring the zone of microbial staining around the rim of the brine pool, the black-colored bivalve *A. muriatica* pervasively inhabits a 20-cm-thick zone above the brine-seawater interface. Seemingly agnostic to substrate, the density of this suspension-feeding bivalve, first described in the Red Sea<sup>11</sup>, is equal on soft sediment and atop the breccia blocks which have tumbled to straddle the brine surface (e.g., Figs. 2d, 5a, 9e, g). Positioning itself as such, *A. muriatica* is presumed to capitalize on the mixing of brine with ambient seawater which delivers a niche characterized by high salinity, low oxygen, lowered pH, and modestly warmer temperature, as compared to ambient. So located, it might be assumed that these bivalves, and, indeed, the wider metazoan assemblage which associates with the NEOM Brine Pools, are nutritionally sustained by the chemosynthetic activities of the microbial community which inhabit the rim of the pools and their waters. No other live metazoans were observed in the sediments collected with the bivalves, which therefore seem to exclusively inhabit the microbially-rich sediment along the edges of the pools. The same distribution of this bivalve has been reported by Oliver et al.<sup>11</sup> around the rim of the Valdivia Deep brine pool which

situates at a depth of 1525 m on the axial trough of the central Red Sea.

**Pool-associated microbial communities.** By means of 16S rRNA sequencing, the microbial communities inhabiting the upper 20 mm of the five cores transecting the eastern margin of the main NEOM pool were quantified (Fig. 10). The outermost core in the transect (Core #1) penetrated the hemipelagic mud constituting the broader seabed of the Aragonese Deep. The microbial assemblage in Core #1 is dominated by lineages of Gammaproteobacteria, Thaumarchaeota Alphaproteobacteria, and Nitrospira with known aerobic metabolisms. The second core, which sampled seabed darkened in color by a rich microbial fabric (the gray zone), boasted a similar community, again dominated by Gammaproteobacteria and aerobic metabolic capabilities. By contrast, the microbes identified in Core #3, which penetrated the orange swash zone situated immediately outboard of the brine-seawater interface, showed fewer members of likely aerobic taxa, and increased abundances of a broad spectrum of microbes with metabolisms spanning sulfate reduction, methanogenesis, reductive dechlorination, and fermentation. These anaerobic prokaryotes dominate the total community sequenced in the final pair of cores (#4 and #5) which penetrated the bed of the main brine pool. The abundance of sulfate reducers occupying the bed sediments of the pool squares with the depleted  $\text{SO}_4^{2-}/\text{Cl}^-$  ratio measured within the overlying brine (Fig. 6a).

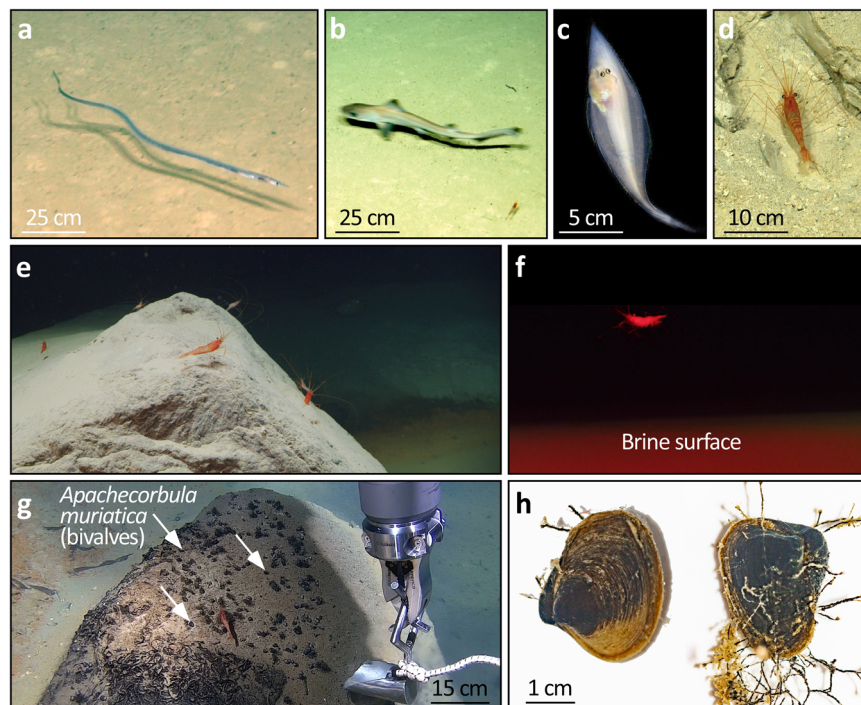


**Fig. 9** Mega- and macrofauna of the NEOM pools. In **a**, an eel, possibly *Ariosoma mauritianum*, swims over the periphery of the main pool in the vicinity of a ubiquitously present bigeye houndshark *Iago omanensis* (**b**). **c** As yet unidentified flat fish, possibly a sharpnose tonguesole *Cynoglossus acutirostris*, collected while it was encountered skimming the brine surface. **d** A common component of the pool's megafauna, the shrimp *Plesionika* sp. (Pandalidae), a species which congregates abundantly atop topographic highs overlooking the pools (**e**). Red light illumination allows the natural behavior of this species to be observed (**f**). Here, a *Plesionika* sp. is encountered >30 m from the edge of the main brine pool, just above the brine surface. Observed behavior consistent with scavenging—this individual and others were recorded retrieving metazoans shocked or killed by the brine. The bivalve *Apachecorbula muriatica* pervasively inhabits a 20-cm-thick zone above the brine-seawater interface. In **g**, this narrow zone falls on a slope-sourced breccia block. **h** Sampled *A. muriatica* in close-up. Note abundant production of byssus thread with multiple split terminations—a characteristic of this species.

## Discussion

Six weeks of submersible and ROV dives to the bathyal depths of the Gulf of Aqaba revealed a desolate seabed thickly draped with mud. As is typical for bathyal and abyssal plains, species diversity is low. The NEOM Brine Pools stand in stark contrast to this monotony. At the periphery of the pools, the interface between normal marine waters and the anoxic brine delivers a niche in which a rich microbial community develops, stratified by the preferred metabolisms of its occupants. As the brine is approached and beneath it, the hypersaline anoxic environment favors extremophile prokaryotes. Among these, the metabolism of sulfate-reducing bacteria delivers brine with the lowest sulfate/chloride ratio yet documented in the Red Sea-Gulf of Aqaba system.

The microbial diversity of the NEOM pools is broadly representative of those identified by equivalent studies in Red Sea brine pools associated with the coastal shelf<sup>12,32</sup>, as well as those pools situated on the axial spreading ridge<sup>13–16,49–51</sup>. Similarities between the NEOM microbial assemblage and these other studies include bacterial classes dominated by KB1, Bacteroidia, Clostridia, Deltaproteobacteria, and Gammaproteobacteria and Archaeal classes dominated by Methanobacteria and Thaumarchaeota<sup>16,32,52</sup>. Perhaps an esoteric ecosystem on face value, subsea hypersaline anoxic brine pools are of broad interest since they arguably represent the most extreme habitable environments on Earth. Indirectly or directly sustained by the chemosynthetic activities of the microbial community, a rich metazoan assemblage spanning, fish, crustacea, and mollusks associate with the pools. Given their high biodiversity, we believe our discovery of the NEOM Brine Pools is prescient—the coastline of the Gulf of Aqaba is rapidly urbanizing<sup>53,54</sup>. This

bathyal ecosystem should be afforded the same protection as the vibrant shallow-water reefs which situate 1.7 km above the pools.

The long core through the bed of the main brine pool reveals a stratigraphy that partitions into three broad modes of deposition. Visually prominent because of their rose color and coarse texture are the siliciclastic intervals. Our core records ten such intervals in the last 1000 years (i through x, Fig. 8). Whatever mechanism delivers these intervals, reoccurs with a frequency of approximately once per century. Of the ten, Interval “v”, dating to ~600 yrs. BP is the thickest (30 cm).

The angular siliciclastic clasts comprising these coarse intervals cannot have been sourced from the marine slope. Shallowing from 200 m depth, submersible dives confirmed that the slope adjacent to the NEOM pools is dominated by mesophotic and then photic reef communities and the calcareous detritus that they yield. Deeper than 200 m, the slope is thickly draped with calcareous mud. We, therefore, posit that these coarse siliciclastic grains are terrigenous, likely deposited into the pool instantaneously as high-density sediment gravity flows—turbidites—an interpretation supported by the upwards-fining composition of these layers and subtle sole marks at their base.

There are only five mechanisms capable of transporting large quantities of terrigenous material downslope into the deep basin (and into the brine pool). Of these, three can be easily discounted. First, permanent rivers—of which none drain into the (hyper-arid) Gulf of Aqaba. Eolian deposition can be discounted too. The grains that comprise the siliciclastic intervals are too coarse to be transported by wind (>80% of grains in these intervals are between  $-1.0$  and  $-2.0$  phi, Fig. 8a). Third, are storm waves impacting the shoreline—the narrow Gulf of Aqaba lacks the fetch to build long-period waves exceeding 2 m in height<sup>55</sup>—too



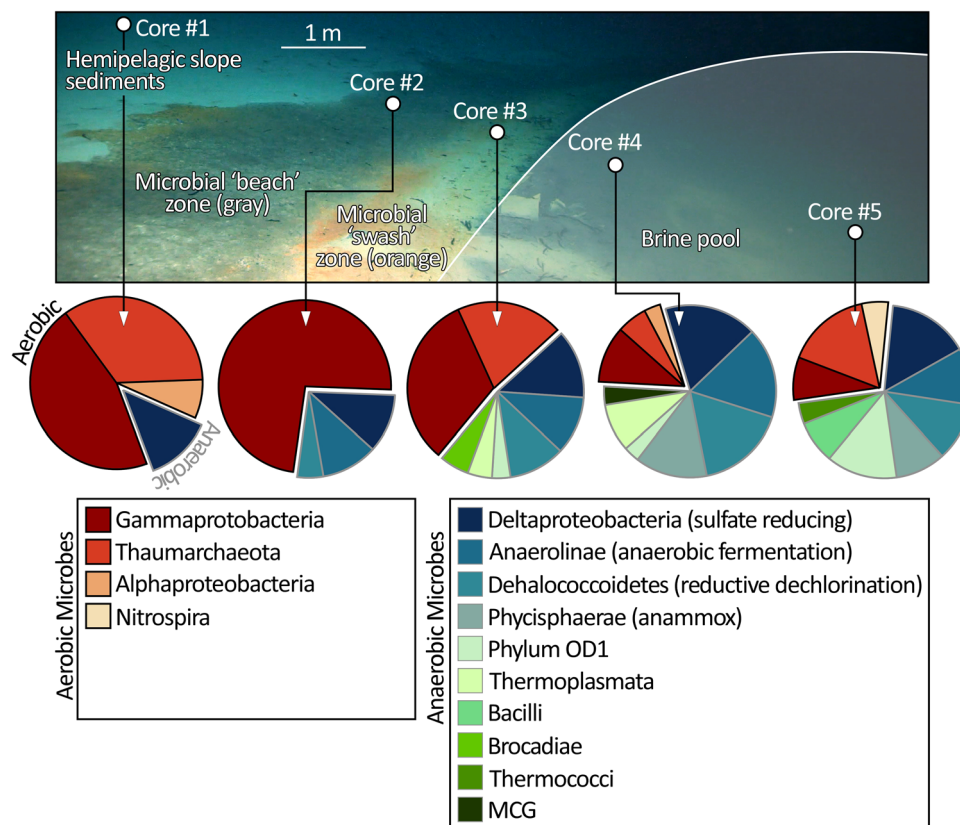


**Fig. 10 Lateral distribution of prokaryote communities comprising 70% of total abundance in and around the main NEOM Brine Pool.** 16S rRNA sequencing of the top 20 mm of the five cores reveal that the microbes inhabiting the background sediment (Core #1) and gray microbial beach zone (Core #2) are dominated by aerobic metabolic capabilities. Moving closer to the shoreline of the pool, this distribution between aerobic and anaerobic metabolisms is reversed in the orange microbial swash zone. For the samples obtained from within the brine pool (Cores #4 and #5), the sequenced microbes are dominated by a diverse suite of anaerobes with metabolisms spanning sulfate reduction, methanogenesis, reductive dechlorination, and fermentation.

small to be a credible means of moving substantial amounts of terrigenous material into the deep basin.

Another possibility is that the terrigenous sediments have been carried from the coastal plain by flashfloods in ephemeral rivers (wadis) triggered by episodic rainfall, as described in Katz et al.<sup>56</sup>; wherein flashfloods generated underwater hyperpycnal flows. However, the size of the sediments within the coarse horizons in our core exceeds what would be anticipated from flood deposition, even with such gravity flows, for several reasons. First, initial flood deposits and associated hyperpycnal plume turbidity currents consist of a wide range of grain sizes but are dominated by weight/volume by fine (<63  $\mu\text{m}$ ) sediments, and only coarsen post-deposition due to resuspension and winnowing<sup>57,58</sup>; processes that are better preserved in the sediment record during prolonged drought phases<sup>59</sup>. In addition, this coarsening via winnowing requires bioturbation, or other such sediment disturbance mechanisms, to resuspend and free the finer sediments for transport further downslope. Therefore, such repeated coarse-grained horizons, as seen in the brine pool core, are: (i) in a context that lacks the mechanisms of bioturbation and resuspension to result in post-depositional coarsening of flashflood deposits, (ii) the coarseness of the horizons exceed the relative sizing of 'coarse' that winnowing would create at these depths, and (iii), if coarse flood deposits are a reflection of drought phases, there is no parallel record suggesting ten independent drought phases in the past millennium.

The second mechanism, to our minds the most plausible, is that the coarse intervals in our core are tsunamites—terrigenous

deposits entrained and transported from the coastal plain by tsunami waves. The coarseness and character of the sand lenses are similar to those described in offshore tsunami deposits in the northernmost portion of the Gulf of Aqaba<sup>60</sup>. This second interpretation bears consideration given that the calibrated  $^{14}\text{C}$  age of the youngest coarse interval in the core, 50 yr. BP closely corresponds to the 1995 Nuweiba earthquake ( $M_w = 7.1$ )<sup>37–39,41</sup>. This earthquake occurred along the Aragonese fault within the Aragonese Deep, the small pull-apart basin in which the NEOM Brine Pools locate, generating a modest tsunami<sup>42</sup>. The ~20 yr. age discrepancy between the 1995 Nuweiba earthquake and the 50 yr. BP  $^{14}\text{C}$  age of the youngest terrigenous core interval is well within the range of error for radiometric dating, especially considering the limited calibration of the  $^{14}\text{C}$  method for material younger than 100 yr. BP. The 1969 Shadwan earthquake ( $M_w = 6.8$ ) was also likely tsunamigenic<sup>61</sup>. Purkis et al.<sup>62</sup> propose that tsunamis are a pervasive fixture in the Gulf, generated both by coseismic seabed deformation and submarine landslides. Being narrowly confined, the authors stress how the Gulf of Aqaba behaves differently from an open ocean in terms of tsunami propagation and impact. Only 80 km to the south of the NEOM Brine Pool, Purkis et al.<sup>62</sup> reports on an incipient submarine landslide in the Tiran Straits which occurred 500–600 yr. BP, possibly spawning a substantial tsunami that, computer simulation would suggest, radiated to the north, up the Gulf of Aqaba, impacting the coastline inboard of the NEOM pools. The timing of this tsunami broadly corresponds to the deposition of the thickest sand lens in the core (Interval "v", Fig. 8). Farther to the

north, evidence from Eilat alludes to a major tsunami dating to 2.3 ka BP<sup>60,63</sup> and deposits on the Egyptian coast have been proposed as tsunamigenic<sup>64</sup>, though their timing is equivocal. The available evidence hence supports the episodic generation of tsunamis in the Gulf of Aqaba.

More than half of the length of the 135 cm core through the bed of the brine pool consists of stacked fining-upward strata which we also interpret as turbidite beds, albeit less dramatic than the exceptionally coarse deposits considered in the previous section. These intervals, which are finer-grained and more numerous, present as classic Bouma sequences, as would be deposited during waning flow as turbidity currents move downslope and out over the brine pool. These sequences span thicknesses of mm to cm, with a base of very-fine to fine-siliciclastic sands, fining upwards to silt or clay (Fig. 8e). We consider these fine-grained fining-upward turbidites to be consistent with the hyperpycnites described by Katz et al.<sup>56</sup> farther north in the Gulf of Aqaba, deposited by muddy submarine hyperpycnal flows generated by flashfloods. These flows (filmed underwater by Katz et al.<sup>56</sup>) originate from the terrestrial discharge of sediment-laden flood waters from wadis during short-lived rain events (hours). As proposed by Parsons et al.<sup>65</sup>, even if a flashflood was to yield a freshwater plume with a density equal to or less than that of the normal marine waters of the Gulf, (i.e., a homopycnal flow), the sediment load contained within it would still be abruptly deposited into the brine by virtue of the convective instability generated by particle settling. This mechanism is important as ensures that flashfloods deposit Bouma sequences into the brine pool, regardless of the bulk density of the freshwater plume. Flashfloods in the Gulf of Aqaba may occur at a frequency of between several times in a year to once every several decades<sup>56,66</sup>, corroborating a large number of stacked fine-grained turbidites in the core. There are at least 50 such fining-upward sequences in the core, corresponding to a reoccurrence frequency of at least four times per century.

Situating along the Arona Fault and only 5 km away from the Aragonese Fault (which slips often—as attested to by the 1995 Nuweiba earthquake and associated aftershocks), the NEOM Brine Pools must experience frequent seismicity. At three intervals, contorted beds were recognized in the core (Fig. 8c, e), consistent with seismic disturbance. Bosworth et al.<sup>35</sup> documents the epicenters of at least 15 earthquakes situated within 50 km of the pool between 1960 and 2016, of which two exceeded  $M_w = 5.0$ . In 1993 alone, Hofstetter<sup>40</sup> meanwhile identified an earthquake swarm of over 420 events to have occurred within and nearby the Aragonese Deep. Induced by such seismicity, rates of footwall uplift for the Saudi coastal terrace adjacent to the pool exceed 0.010 cm/yr when averaged over the last 125 ka<sup>35</sup>. Records assembled by Ambraseys<sup>67</sup> confirm abundant seismicity in the Gulf of Aqaba extending as far back as 1517 when the Ottomans began their 350-year administration of Egypt. Even minor shaking should be expected to induce downslope movement of sediments, particularly given that the foreslope adjacent to the pool is both the steepest ( $>35^\circ$ ) and deepest ( $>1700$  m) in the entire Gulf of Aqaba (Fig. 3b). Configured as such, the brine pool is likely the frequent recipient of seismically-induced turbidite deposits—seismites. Separating hyperpycnites (flashflood deposits) from seismites lies beyond the scope of this paper, but will be tackled by comparing the historical earthquake record of the Gulf with the dated deposits in our core.

Even the sharp salinity gradient which demarks the surface of the brine pool (Fig. 4) might owe itself to seismicity. Though we admit that the vertical fidelity of our salinity measurement is insufficient to speak definitively, this gradient appears sharper than the normal diffusion profile which would be expected had the pool reached a steady state with the body of normal seawater

which overlies it. Such a sharp gradient might indicate the recent and abrupt emplacement of brine as could be mediated, for example, by the movement of the Arona fault, on which the pool sits. This possibility emphasizes the value of repeated measurement through the time of the NEOM brine. For instance, as has been achieved for the pools of the Atlantis II Deep axial depression in the Red Sea<sup>4</sup>.

Whereas other brine pools in the Red Sea and Gulf have been cored<sup>12,17,68–70</sup>, none are sufficiently close to the shore to receive the terrestrial sediments that can serve to record coastal processes. Although event beds from tsunamis, flashfloods, and seismicity would be deposited abundantly at the toe-of-slope in the Aragonese Deep, the NEOM pools offer exceptional conditions conducive to their intricate preservation. First, because of the anoxic brine, epibenthic megafauna is eliminated from the pools and bioturbation is entirely absent. This stands in stark contrast to the many cores that have been retrieved away from brine pools in the Gulf of Aqaba which are heavily bioturbated<sup>60,71,72</sup>. Second, the high density of the brine effectively shields the bed from deep-water currents (contourites) which would otherwise winnow or erode the bathyal seabed.

The third exceptional property of the pools is the way that descending turbidites will interact with the brine prior to depositing on the bed of a pool. As can be visualized via the injection of dye (Fig. 2c), the seawater-brine interface delivers a stark density gradient. Indeed, so dense is the brine that we could land our 10,000 lb ROV on its surface to choreograph deployment of the CTD (Fig. 2b). Upon reaching the surface of the brine, this density gradient would be sufficient to temporarily arrest a turbidity current, the material from which would then settle through the brine to deposit on the seabed, with the dense grains settling swiftest, and so on, until the finest grains settle last, capping the fining-upward interval. Since the energy of the descending turbidite would not immediately reach the pool's bed (it would instead be absorbed by the seawater-brine interface), the plume would not scour, disturb, or destroy the sediments deposited by previous events. In this way, even layers with mm-scale Bouma sequences are delicately preserved in the base of the pool, potentially delivering an exquisite long-term record of tsunamis, flashfloods, and seismicity in the area. We hence believe that the brine pools have a remarkable property that might commend them to both paleoclimatologists and to seismologists.

## Conclusions

Analysis and characterization of the NEOM Brine Pools have resulted in the establishment of the first examples in the greater Red Sea system to be located sufficiently close to the coastline to act as sediment deposition traps for slope processes. Situated as such, the NEOM pools have a unique potential to archive historical tsunamis, flashfloods, and seismicity in the Gulf of Aqaba on millennial timescales. By ascertaining that brine pools form outside the rifting portion of the Red Sea, in the Gulf of Aqaba, we hope to have expanded the notion of how brine pools are formed and where. For the first time, we have also emphasized the value of brine pools as sediment archives, by revealing a multi-phase, multi-event sequence of sedimentary deposits preserved beneath the NEOM pools.

## Methods

**Swath multibeam, sonar, and ROV.** Building forward from mapping published by Ribot et al.<sup>34</sup>, the 2020 OceanX “Deep Blue” Expedition acquired a comprehensive geophysical dataset spanning the northern Red Sea and Gulf of Aqaba. The expedition was conducted aboard OceanXplorer, an 87 m research vessel furnished with state-of-the-art tools for seabed mapping, including a pair of custom Triton submersibles with a diving depth of 1000 m, plus a 6000-m-rated Argus Mariner XL remotely operated vehicle (ROV). These assets were used exhaustively throughout the 6-week expedition to collect seabed and water samples, cores, and

geophysical data encompassing bathymetry, sub-bottom, and ADCP (acoustic Doppler current profiler) profiles. Key to supporting this study is the swath multibeam data acquired using hull-mounted Kongsberg EM712 and EM304 systems operating in the 70–100 kHz range calibrated with CTD (conductivity, temperature, depth) and expendable bathythermograph (XBT) profiles. The beam density of these systems was configured to deliver a minimum across-track resolution of 10 m. Upon discovery of the pools, we conducted a series of ROV dives to map their geometry, obtain samples, and acquire high-resolution digital video and still footage (Fig. 2). The pools lacked a multibeam signature but, by virtue of their dampened backscatter as compared to the surrounding seabed, were detected by the ROV-mounted 450–900 kHz imaging sonar, aiding navigation, and mapping.

**Sampling the brine.** We lowered a Sea-Bird 911+ CTD system equipped with a rosette of 12 × 12 L Niskin bottles into the main brine pool at 28° 47.31587'N, 34° 47.70937'E. For each multiple cast, the rosette was triggered to obtain water samples 500 and 5 m above the seawater–brine interface, at the interface, and below it (Fig. 2b – see also Supplementary Data 1). Simultaneously, we collected vertical profiles of salinity, dissolved oxygen, and temperature (Fig. 4). Spot soundings confirmed that the center of the pool was 6 m deep, allowing for the Sea-Bird to be completely submerged in the brine. So dense was the brine surface, that the ROV could “land” on the brine surface and the CTD casts were choreographed in real-time from the vehicle’s high-definition video stream.

The salinity of these water samples was determined using a refractometer, the oxygen isotopes ( $\delta^{18}\text{O}$ ) using a Picarro cavity ring-down spectrometer, and chloride using titration with 0.1 silver nitrate using potassium permanganate as an end-point indicator and calibrated using IAPSO (International Association for the Physical Sciences of the Oceans) standard seawater. Total alkalinity and initial pH were measured following the workflows published by Gieskes et al.<sup>73</sup> which employs a potentiometric titration of acid handled online by a computer interfaced with a pH meter and a Metrohm autoburette. Elemental concentrations were measured on an Agilent 8900 ICP-MS/MS after samples were diluted by factors proportional to their salinity. SPEX CertiPrep multielement solutions, IAPSO, and CASS-6 were used as certified reference materials.

**Cores, CT, and a radiocarbon age model for the brine pool.** A transect of five cores was acquired across the western rim of the main brine pool to sample the four concentric microbially-stained zones which develop around its rim (Fig. 7). Using the ROV’s hydraulic manipulator arm, each of the four zones was sampled with a 50 cm push core (Cores #1 through 4), plus one additional long core (150 cm) was pushed into the sediments accumulating beneath the brine (Core #5).

The long core was scanned via computed tomography (CT) to reconstruct its three-dimensional lithology. The CT data were processed with the ZIB edition of the Amira software [v. 2021.03<sup>74</sup>] to yield maps of grain size, clast distribution, and orthoslices. A full description of this processing stream is given in Supplementary Materials (S1).

Following CT scanning, pore waters were extracted from the cores via drilling through their liners at 25 mm increments and inserting Rhizon samplers which filter samples to 0.22  $\mu\text{m}$ <sup>75</sup>. The recovered pore volumes ranged in volume from 5–15  $\text{cm}^3$ , and samples were immediately analyzed for alkalinity, salinity, and chloride concentration. Prior to elemental analysis, 0.5  $\mu\text{l}$  of 5% UT  $\text{HNO}_3$  was added to aliquots of porewater, brine, and seawater samples, and stored at 4 °C. With their pore waters extracted, the cores were sliced to enable sedimentological description and physical sampling for geochemistry, mineralogy, genomic analyses, and radiometric dating.

As detailed in Supplementary Materials, S2, radiocarbon ( $^{14}\text{C}$ ) dating was conducted on the long core acquired from the center of the brine pool. Six samples were extracted at prominent stratigraphic horizons (Fig. S2) and submitted to Beta Analytic Inc. for dating. These ages and their associated uncertainties were calibrated against the current marine calibration curve [Marine20<sup>76</sup>] using the Calib8.2 online platform<sup>77</sup>. To calibrate the  $^{14}\text{C}$  dates against Marine20, a local value for the regional-marine radiocarbon reservoir age correction ( $\Delta\text{R}$ ) is required. The  $\Delta\text{R}$  for the Gulf of Aqaba was calculated following Reimer and Reimer<sup>78</sup> using the average U-Th age for a mesophotic coral sample collected in the southern Gulf<sup>62</sup>. At the 95% confidence range, the local  $\Delta\text{R}$  of  $-44 \pm 74$  was used to account for the marine radiocarbon reservoir age corrections. The calibrated  $^{14}\text{C}$  ages are reported as the calibrated year before present (cal. yr. BP)— Supplementary Data 1.

The original length of the long core, 135 cm, was compressed to 85 cm during acquisition. Before attempting to construct the age model, the length of the core and the position of sub-samples for radiocarbon dating was adjusted to the original length of the core. An age-depth model was constructed based on a Bayesian approach using the “Bchron” package<sup>46,47</sup> (<https://cran.r-project.org/web/packages/Bchron/index.html>). We used the “accumulation” output field in Bchron to create sedimentation rates for the sediment core (Fig. S2), defined as the thickness of sediment accumulated during a given unit of time in mm/yr. Several layers deemed to have been deposited by high-density grain flows with different thicknesses, ranging from 1 to 300 mm, were identified along the core, which are indicative of rapid deposition during a very short time. Deposition of these layers were not incorporated in our calculation of sedimentation rates. As a result, the presented sedimentation rates (Fig. S2) should be considered as overall rates. In a different approach, we also calculated the linear sedimentation rates between

radiocarbon tie points to provide a more detailed sedimentation rate for the core (Fig. S2). Similarly, deposition of layers with high-density grain flows were not incorporated in this approach.

**X-ray fluorescence and X-ray diffraction scanning.** X-ray fluorescence (XRF) data were acquired using the Avaatech XRF core scanner at the University of Miami. Full procedures and scan settings are provided in Supplementary Materials, section S3 (and see Supplementary Data 1). We capitalize on the XRF results to diagnose the provenance of the stratigraphic horizons recognized in the long core through the brine pool (Fig. 8j–l). Heavy minerals in siliciclastic sediments are enriched in zirconium (Zr)<sup>79</sup>. Consequently, in marine cores, Zr abundance can be used to proxy coarse siliciclastic intervals in a sedimentary profile<sup>80</sup>. In a similar vein, Rubidium (Rb) often appears in potassium silicates, such as K-feldspar, illite, and muscovite, and may be used as a measure of amounts of clay material or coarse-grain K-feldspar present in the sedimentary record<sup>79,81</sup>. Iron (Fe) and potassium (K) are elements related to aluminosilicate minerals, such as K-feldspar and biotite, and associate with the input of terrigenous sediment into marine basins<sup>82–88</sup>. Whereas strontium (Sr) can be associated with feldspar and biotite<sup>82</sup>, the concentrations are low, and this element primarily associates with the carbonate fraction of sedimentary successions, particularly calcite and aragonite, owing to the substitution of Sr for Ca within the carbonate lattice.

To determine mineralogy, X-Ray Diffraction (XRD) was conducted on powdered samples extracted at 25 mm intervals down the cores. Full details of this analysis are provided in Supplementary Materials, section S4. Results from XRD facilitated the calculation of the percentage of feldspar and quartz (Fig. 8m), thereby identifying the coarsest intervals in the core as siliciclastic.

**Stable isotope geochemistry.** As treated in detail in Supplementary Materials (S5), stable isotopes analysis of the carbon and nitrogen in the organic matter were also conducted at 25 mm intervals down the cores using a Finnigan-MAT 251 mass spectrometer (Fig. 8n). This analysis also yielded the percentages of organic carbon and nitrogen after decalcification with dilute HCl (Fig. 8o). These data (Supplementary Data 1) were used to identify the source of organic matter in the sediments which have accumulated in the brine pool.

**16S rRNA sequencing of core tops.** To prevent contamination, the thin surface layer was removed from each of the five cores. Next, the upper 20 mm of each core was sampled for their microbial communities using 16S rRNA sequencing. For the sake of brevity, full detail on the extraction of genomic DNA is relegated to Supplementary Materials (S6). Data provided as Supplementary Data 1. The fidelity of the sequencing was sufficient to identify seven classes of prokaryotes whose per-core relative abundances were tallied to reveal gradients in the prokaryotic community in and around the brine pool. We acknowledge that the high salinity of the brine which infuses the sampled sediments can deliver preservation effects, such that some of the biodiversity captured by our molecular methods might represent ‘pickled’ rRNA, rather than active living members of the microbial community.

## Data availability

The authors confirm that the data supporting the findings of this study are available within the article and its supplementary materials. These data are additionally available online: <https://zenodo.org/record/6570649#.YoprSKjMjQR> (<https://doi.org/10.5281/zenodo.6570649>)<sup>89</sup>.

Received: 4 March 2022; Accepted: 16 June 2022;

Published online: 27 June 2022

## References

1. Backer, H. & Schoell, M. New deeps with brines and metalliferous sediments in the Red Sea. *Nat. Phys. Sci.* **240**, 153–158 (1972).
2. Aharon, P., Roberts, H. H. & Snelling, R. Submarine venting of brines in the deep Gulf of Mexico: observations and geochemistry. *Geology* **20**, 483–486 (1992).
3. Woodside, J. M. & Volgin, A. V. Brine pools associated with Mediterranean Ridge mud diapirs: an interpretation of echo-free patches in deep tow sidescan sonar data. *Mar. Geol.* **132**, 55–61 (1996).
4. Anschutz, P., Blanc, G., Chatin, F., Geiller, M. & Pierret, M.-C. Hydrographic changes during 20 years in the brine-filled basins of the Red Sea. *Deep Sea Res. I: Oceanogr. Res. Pap.* **46**, 1779–1792 (1999).
5. Cita, M. B. Exhumation of Messinian evaporites in the deep-sea and creation of deep anoxic brine-filled collapsed basins. *Sediment. Geol.* **188**, 357–378 (2006).
6. Schmidt, M., Al-Farawati, R. & Botz, R. In *The Red Sea* (Rasul, N. M. A. & Stewart, I. C. F.) Ch. 13 (Springer, 2015).

7. Sawyer, D. E., Mason, R. A., Cook, A. E. & Portnov, A. Submarine landslides induce massive waves in subsea brine pools. *Sci. Rep.* **9**, 1–9 (2019).
8. Vanreusel, A. et al. Biodiversity of cold seep ecosystems along the European margins. *Oceanography* **22**, 110–127 (2009).
9. Vestheim, H. & Kaartvedt, S. A deep sea community at the Kebrit brine pool in the Red Sea. *Mar. Biodivers.* **46**, 59–65 (2016).
10. Lazar, C. S. In *Marine Hydrocarbon Seeps* (Teske, A. & Carvalho, V.) Ch. 6 (Springer, 2020).
11. Oliver, P. G., Vestheim, H., Antunes, A. & Kaartvedt, S. Systematics, functional morphology and distribution of a bivalve (*Apachecorbula muriatica* gen. et sp. nov.) from the rim of the ‘Valdivia Deep’ brine pool in the Red Sea. *J. Mar. Biol. Assoc. UK* **95**, 523–535 (2015).
12. Wang, Y. et al. Diversity and distribution of eukaryotic microbes in and around a brine pool adjacent to the Thuwal cold seeps in the Red Sea. *Front. Microbiol.* **5**, 37 (2014).
13. Eder, W., Jahnke, L. L., Schmidt, M. & Huber, R. Microbial diversity of the brine-seawater interface of the Kebrit Deep, Red Sea, studied via 16S rRNA gene sequences and cultivation methods. *Appl. Environ. Microbiol.* **67**, 3077–3085 (2001).
14. Antunes, A., Ngugi, D. K. & Stingl, U. Microbiology of the Red Sea (and other deep-sea anoxic brine lakes). *Environ. Microbiol. Rep.* **3**, 416–433 (2011).
15. Ngugi, D. K. et al. Comparative genomics reveals adaptations of a halotolerant thaumarchaeon in the interfaces of brine pools in the Red Sea. *ISME J.* **9**, 396–411 (2015).
16. Merlino, G., Barozzi, A., Michoud, G., Ngugi, D. K. & Daffonchio, D. Microbial ecology of deep-sea hypersaline anoxic basins. *FEMS Microbiol. Ecol.* **94**, fiy085 (2018).
17. Siam, R. et al. Unique prokaryotic consortia in geochemically distinct sediments from Red Sea Atlantis II and discovery deep brine pools. *PLoS ONE* **7**, e42872 (2012).
18. Eder, W., Schmidt, M., Koch, M., Garbe-Schönberg, D. & Huber, R. Prokaryotic phylogenetic diversity and corresponding geochemical data of the brine-seawater interface of the Shaban Deep, Red Sea. *Environ. Microbiol.* **4**, 758–763 (2002).
19. Mancinelli, R., Fahlen, T., Landheim, R. & Klovstad, M. Brines and evaporites: analogs for Martian life. *Adv. Space Res.* **33**, 1244–1246 (2004).
20. Van Der Wielen, P. W. et al. The enigma of prokaryotic life in deep hypersaline anoxic basins. *Science* **307**, 121–123 (2005).
21. Ziko, L., Adel, M., Malash, M. N. & Siam, R. Insights into Red Sea brine pool specialized metabolism gene clusters encoding potential metabolites for biotechnological applications and extremophile survival. *Mar. Drugs* **17**, 273 (2019).
22. Sagar, S. et al. Induction of apoptosis in cancer cell lines by the Red Sea brine pool bacterial extracts. *BMC Complement. Altern. Med.* **13**, 1–12 (2013).
23. Craig, H. In *Hot Brines and Recent Heavy Metal Deposits in the Red Sea* (Degens, E. T. & Ross, D. A.) Ch. 3 (Springer, 1969).
24. Mart, Y. & Ross, D. A. Post-Miocene rifting and diapirism in the northern Red Sea. *Mar. Geol.* **74**, 173–190 (1987).
25. Ehrhardt, A., Hübscher, C., Ben-Avraham, Z. & Gajewski, D. Seismic study of pull-apart-induced sedimentation and deformation in the Northern Gulf of Aqaba (Elat). *Tectonophysics* **396**, 59–79 (2005).
26. Purkis, S. J., Harris, P. M. & Ellis, J. Patterns of sedimentation in the contemporary Red Sea as an analog for ancient carbonates in rift settings. *J. Sediment. Res.* **82**, 859–870 (2012).
27. Mitchell, N. C., Shi, W., Izzeldin, A. & Stewart, I. C. Reconstructing the level of the central Red Sea evaporites at the end of the Miocene. *Basin Res.* **33**, 1266–1292 (2021).
28. Orszag-Sperber, F., Harwood, G., Kendall, A. & Purser, B. In *Sedimentation and Tectonics in Rift Basins Red Sea: Gulf of Aden* (Purser, B. H. & Bosence, D. W.) Ch. F1 (Springer, 1998).
29. Ross, D. & Hunt, J. Third brine pool in the Red Sea. *Nature* **213**, 687–688 (1967).
30. Schardt, C. Hydrothermal fluid migration and brine pool formation in the Red Sea: the Atlantis II Deep. *Miner. Deposita* **51**, 89–111 (2016).
31. Batang, Z. B. et al. First discovery of a cold seep on the continental margin of the central Red Sea. *J. Mar. Syst.* **94**, 247–253 (2012).
32. Duarte, C. M. et al. Discovery of Afifi, the shallowest and southernmost brine pool reported in the Red Sea. *Sci. Rep.* **10**, 1–17 (2020).
33. Augustin, N., Van der Zwan, F. M., Devey, C. W. & Brandsdóttir, B. 13 million years of seafloor spreading throughout the Red Sea Basin. *Nat. Commun.* **12**, 1–10 (2021).
34. Ribot, M. et al. Active faults’ geometry in the Gulf of Aqaba, Southern Dead Sea Fault, illuminated by multibeam Bathymetric data. *Tectonics* **40**, e2020TC006443 (2021).
35. Bosworth, W., Montagna, P., Pons-Branchu, E., Rasul, N. & Taviani, M. Seismic hazards implications of uplifted Pleistocene coral terraces in the Gulf of Aqaba. *Sci. Rep.* **7**, 1–13 (2017).
36. Hartman, G. et al. Quaternary tectonic evolution of the Northern Gulf of Elat/Aqaba along the Dead Sea Transform. *J. Geophys. Res. Solid Earth* **119**, 9183–9205 (2014).
37. Abdel-Fattah, A. K., Hussein, H. M., Ibrahim, E. M. & El Atta, A. A. Fault plane solutions of the 1993 and 1995 Gulf of Aqaba earthquakes and their tectonic implications. *Ann. Geophys.* **40**, 1555–1564 (1997).
38. Baer, G., Sandwell, D., Williams, S., Bock, Y. & Shamir, G. Coseismic deformation associated with the November 1995, Mw= 7.1 Nuweiba earthquake, Gulf of Elat (Aqaba), detected by synthetic aperture radar interferometry. *J. Geophys. Res. Solid Earth* **104**, 25221–25232 (1999).
39. Klinger, Y., Rivera, L., Haessler, H. & Maurin, J.-C. Active faulting in the Gulf of Aqaba: new knowledge from the Mw 7.3 earthquake of 22 November 1995. *Bull. Seismol. Soc. Am.* **89**, 1025–1036 (1999).
40. Hofstetter, A. Seismic observations of the 22/11/1995 Gulf of Aqaba earthquake sequence. *Tectonophysics* **369**, 21–36 (2003).
41. Tibor, G. et al. Active tectonic morphology and submarine deformation of the northern Gulf of Eilat/Aqaba from analyses of multibeam data. *Geo-Marine Letters* **30**, 561–573 (2010).
42. Frucht, E. et al. A fresh view of the tsunami generated by the Dead Sea Transform, 1995 Mw 7.2 Nuweiba earthquake, along the Gulf of Elat–Aqaba. *Seismol. Res. Lett.* **90**, 1483–1493 (2019).
43. Anschutz, P., Turner, J. & Blanc, G. The development of layering, fluxes through double-diffusive interfaces, and location of hydrothermal sources of brines in the Atlantis II Deep: Red Sea. *J. Geophys. Res. Oceans* **103**, 27809–27819 (1998).
44. Swift, S. A., Bower, A. S. & Schmitt, R. W. Vertical, horizontal, and temporal changes in temperature in the Atlantis II and Discovery hot brine pools, Red Sea. *Deep Sea Res. I Oceanogr. Res. Pap.* **64**, 118–128 (2012).
45. Aref, M. A. & Mannaa, A. A. Formation and evolution of efflorescent halite speleothems beneath tepee structures in the Red Sea coastal evaporation settings, Jeddah, Saudi Arabia. *Sediment. Geol.* **414**, 105828 (2021).
46. Haslett, J. & Parnell, A. A simple monotone process with application to radiocarbon-dated depth chronologies. *J. R. Stat. Soc. C Appl. Stat.* **57**, 399–418 (2008).
47. Parnell, A. C., Haslett, J., Allen, J. R., Buck, C. E. & Huntley, B. A flexible approach to assessing synchronicity of past events using Bayesian reconstructions of sedimentation history. *Quat. Sci. Rev.* **27**, 1872–1885 (2008).
48. Lamb, A. L., Wilson, G. P. & Leng, M. J. A review of coastal palaeoclimate and relative sea-level reconstructions using  $\delta^{13}C$  and C/N ratios in organic material. *Earth Sci. Rev.* **75**, 29–57 (2006).
49. Wang, Y. et al. Autotrophic microbe metagenomes and metabolic pathways differentiate adjacent Red Sea brine pools. *Sci. Rep.* **3**, 1–11 (2013).
50. Abdallah, R. Z. et al. Aerobic methanotrophic communities at the Red Sea brine-seawater interface. *Front. Microbiol.* **5**, 487 (2014).
51. Wang, Y. et al. Zonation of microbial communities by a hydrothermal mound in the Atlantis II Deep (the Red Sea). *PLoS ONE* **10**, e0140766 (2015).
52. Guan, Y., Hikmawan, T., Antunes, A., Ngugi, D. & Stingl, U. Diversity of methanogens and sulfate-reducing bacteria in the interfaces of five deep-sea anoxic brines of the Red Sea. *Res. Microbiol.* **166**, 688–699 (2015).
53. Chalastani, V. I. et al. Reconciling tourism development and conservation outcomes through marine spatial planning for a Saudi Giga-Project in the Red Sea (The Red Sea Project, Vision 2030). *Front. Mar. Sci.* **7**, 168 (2020).
54. Rowlands, G., Purkis, S. & Bruckner, A. Tight coupling between coral reef morphology and mapped resilience in the Red Sea. *Mar. Pollut. Bull.* **105**, 575–585 (2016).
55. Abu-Hilal, A. H. & Al-Najjar, T. Litter pollution on the Jordanian shores of the Gulf of Aqaba (Red Sea). *Mar. Environ. Res.* **58**, 39–63 (2004).
56. Katz, T. et al. Desert flash floods form hyperpycnal flows in the coral-rich Gulf of Aqaba, Red Sea. *Earth Planet. Sci. Lett.* **417**, 87–98 (2015).
57. Mathalon, A., Goodman-Tchernov, B., Hill, P., Kálmán, Á. & Katz, T. Factors influencing flashflood deposit preservation in shallow marine sediments of a hyperarid environment. *Mar. Geol.* **411**, 22–35 (2019).
58. Kalman, A., Katz, T., Hill, P. & Goodman-Tchernov, B. Droughts in the desert: Medieval Warm Period associated with coarse sediment layers in the Gulf of Aqaba-Eilat, Red Sea. *Sedimentology* **67**, 3152–3166 (2020).
59. Kalman, A. et al. Anthropogenic changes in waterways produce “drought-like” layers in shelf sediments. *Elem. Sci. Anth.* **10**, 00039 (2022).
60. Goodman Tchernov, B. et al. Offshore evidence for an undocumented tsunami event in the ‘low risk’ Gulf of Aqaba-Eilat, Northern Red Sea. *PLoS ONE* **11**, e0145802 (2016).
61. Ben-Menahem, A. Four thousand years of seismicity along the Dead Sea rift. *J. Geophys. Res. Solid Earth* **96**, 20195–20216 (1991).
62. Purkis, S. J. et al. Tsunamigenic potential of an incipient submarine landslide in the Tiran Straits. *Geophys. Res. Lett.* **49**, e2021GL097493 (2022).
63. Shaked, Y. et al. Large earthquakes kill coral reefs at the north-west Gulf of Aqaba. *Terra Nova* **16**, 133–138 (2004).

64. Salem, E.-S. M. Paleo-tsunami deposits on the Red Sea beach, Egypt. *Arab. J. Geosci.* **2**, 185–197 (2009).
65. Parsons, J. D., Bush, J. W. & Syvitski, J. P. Hyperpycnal plume formation from riverine outflows with small sediment concentrations. *Sedimentology* **48**, 465–478 (2001).
66. Purkis, S. J., Rowlands, G. P., Riegl, B. M. & Renaud, P. G. The paradox of tropical karst morphology in the coral reefs of the arid Middle East. *Geology* **38**, 227–230 (2010).
67. Ambraseys, N. *Earthquakes in the Mediterranean and Middle East: A Multidisciplinary Study of Seismicity up to 1900* (Cambridge Univ. Press, 2009).
68. Adel, M. et al. Viruses-to-mobile genetic elements skew in the deep Atlantis II brine pool sediments. *Sci. Rep.* **6**, 1–9 (2016).
69. Erickson, A. J. & Simmons, G. In *Hot Brines and Recent Heavy Metal Deposits in the Red Sea* (Degens, E. T. & Ross, D. A.) Ch. 2 (Springer, 1969).
70. Hunt, J. M., Hays, E. E., Degens, E. T. & Ross, D. A. Red Sea: detailed survey of hot-brine areas. *Science* **156**, 514–516 (1967).
71. Al-Najjar, T., Rasheed, M., Ababneh, Z., Ababneh, A. & Al-Omarey, H. Heavy metals pollution in sediment cores from the Gulf of Aqaba, Red Sea. *Nat. Sci.* **3**, 775 (2011).
72. Pätzold, J. Report and preliminary results of METEOR Cruise M44/3, Aqaba (Jordan)-Safaga (Egypt)-Duba (Saudi Arabia)-Suez (Egypt)-Haifa (Israel), 12.3.-26.3.-24.-4.4. 1999. *Berichte, Fachbereich Geowissenschaften, Universität Bremen* (2000).
73. Gieskes, J. M., Gamo, T. & Brumsack, H. Chemical methods for interstitial water analysis aboard JOIDES Resolution. *ODP Technical Note 15* (1991).
74. Stalling, D., Westerhoff, M. & Hege, H. C. In *The Visualization Handbook* (Hansen, C. D. & Johnson, C. R.) Ch. 38 (Elsevier, 2005).
75. Dickens, G. R., Koelling, M., Smith, D. C. & Schnieders, L. Rhizon sampling of pore waters on scientific drilling expeditions: an example from the IODP Expedition 302, Arctic Coring Expedition (ACEX). *Sci. Drill.* **4**, 22–25 (2007).
76. Heaton, T. J. et al. Marine20—the marine radiocarbon age calibration curve (0–55,000 cal BP). *Radiocarbon* **62**, 779–820 (2020).
77. Stuiver, M., Reimer, P. & Reimer, R. CALIB 8.2. <http://calib.org> (2021).
78. Reimer, R. W. & Reimer, P. J. An online application for  $\Delta R$  calculation. *Radiocarbon* **59**, 1623–1627 (2017).
79. Fralick, P. & Kronberg, B. Geochemical discrimination of clastic sedimentary rock sources. *Sediment. Geol.* **113**, 111–124 (1997).
80. Dypvik, H. & Harris, N. B. Geochemical facies analysis of fine-grained siliciclastics using Th/U, Zr/Rb and (Zr+ Rb)/Sr ratios. *Chem. Geol.* **181**, 131–146 (2001).
81. Lo, F.-L., Chen, H.-F. & Fang, J.-N. Discussion of suitable chemical weathering proxies in sediments by comparing the dissolution rates of minerals in different rocks. *J. Geol.* **125**, 83–99 (2017).
82. Dean, W. E. & Arthur, M. A. In *SEPM Society for Sedimentary Geology - Concepts in Sedimentology and Paleontology* (Dean, W. E. & Arthur, M. A.) Ch. 13 (Society for Sedimentary Geology, 1998).
83. Martins, V. et al. A multiproxy approach of the Holocene evolution of shelf-slope circulation on the NW Iberian Continental Shelf. *Mar. Geol.* **239**, 1–18 (2007).
84. Mulitza, S. et al. Sahel megadroughts triggered by glacial slowdowns of Atlantic meridional overturning. *Paleoceanography* **23** (2008).
85. Lupker, M., Aciego, S. M., Bourdon, B., Schwander, J. & Stocker, T. Isotopic tracing (Sr, Nd, U and Hf) of continental and marine aerosols in an 18th century section of the Dye-3 ice core (Greenland). *Earth Planet. Sci. Lett.* **295**, 277–286 (2010).
86. Govin, A. et al. Distribution of major elements in Atlantic surface sediments (36 N–49 S): Imprint of terrigenous input and continental weathering. *Geochem. Geophys. Geosyst.* **13** (2012).
87. Burone, L. et al. A multiproxy study between the Río de la Plata and the adjacent South-western Atlantic inner shelf to assess the sediment footprint of river vs. marine influence. *Cont. Shelf Res.* **55**, 141–154 (2013).
88. Perez, L., García-Rodríguez, F. & Hanebuth, T. J. Variability in terrigenous sediment supply offshore of the Río de la Plata (Uruguay) recording the continental climatic history over the past 1200 years. *Clim. Past* **12**, 623–634 (2016).
89. Purkis, S. J. Geochemical and genomic data from the NEOM Brine Pool (Gulf of Aqaba). <https://doi.org/10.5281/zenodo.6570649> (2022).
90. Weatherall, P. et al. A new digital bathymetric model of the world's oceans. *Earth Space Sci.* **2**, 331–345 (2015).

## Acknowledgements

We owe a debt of gratitude to our Saudi Arabian partners, NEOM, and to Paul Marshall for facilitating the Deep Blue Expedition and issuing sampling permits. We are similarly indebted to OceanX and the crew of OceanXplorer for their operational and logistical support for the duration of this expedition. In particular, we would like to acknowledge Olaf Dieckhoff, Ewan Bason, Carmen Greto, and Colleen Peters for data acquisition, sample collection, and support of scientific operations on board OceanXplorer. We would also like to thank OceanX Media, for documenting and communicating this work with the public. Gratitude is extended to three anonymous referees, Derek Sawyer, and to Neil Mitchell for their insightful reviews. We thank Beverly Goodman Tchernov for her advice on an earlier draft of this manuscript. G.C. was supported by the Italian Ministry of Education, University and Research (PON 2014–2020, Grant AIM 1807508-1, Linea 1). This study was funded by NEOM Company under the 2020 NEOM-OceanX Red Sea Expedition.

## Author contributions

S.J.P. conceived the study, led the dive during which the brine pool was discovered, and led the analysis and write-up. F.M., F.B., and G.C. participated in the research cruise and assisted in the interpretation of the discovery and identification of the megafauna. Geochemical analysis was led by P.K.S. and A.O., with assistance from G.D. Sampling for genomics and subsequent interpretation was conducted by H.S. and J.K. X-ray fluorescence of cores was supervised by L.P., CT scanning by G.K., and reconstruction of CT scans by J.T. The radiometric dating was performed by A.S., who contributed to the sedimentology along with G.P.E. Dive planning was overseen by A.C. who also piloted the ROV, under the supervision of OceanX Science Program Lead M.R. Finally, A.A. organized the expedition and led site selection. All authors reviewed the manuscript.

## Competing interests

The authors declare no competing interests.

## Additional information

**Supplementary information** The online version contains supplementary material available at <https://doi.org/10.1038/s43247-022-00482-x>.

**Correspondence** and requests for materials should be addressed to Sam J. Purkis.

**Peer review information** *Communications Earth & Environment* thanks Yong Wang, Derek Sawyer, Neil Mitchell and André Antunes for their contribution to the peer review of this work. Primary Handling Editors: Olivier Sulpis, Joe Aslin.

**Reprints and permission information** is available at <http://www.nature.com/reprints>

**Publisher's note** Springer Nature remains neutral with regard to jurisdictional claims in published maps and institutional affiliations.



**Open Access** This article is licensed under a Creative Commons Attribution 4.0 International License, which permits use, sharing, adaptation, distribution and reproduction in any medium or format, as long as you give appropriate credit to the original author(s) and the source, provide a link to the Creative Commons license, and indicate if changes were made. The images or other third party material in this article are included in the article's Creative Commons license, unless indicated otherwise in a credit line to the material. If material is not included in the article's Creative Commons license and your intended use is not permitted by statutory regulation or exceeds the permitted use, you will need to obtain permission directly from the copyright holder. To view a copy of this license, visit <http://creativecommons.org/licenses/by/4.0/>.

© The Author(s) 2022